Deuterium Trapping Mechanisms in Reduced Activation Ferritic Martensitic Steels and Their Correlation with Mechanical Strengthening

Weicheng Zhong[1,*], Dave Sprouster[2], Mingxi Ouyang[2], Lance L. Snead[2], Yutai Katoh[1].
[1]Material Science and Technology Division, Oak Ridge National Laboratory, Oak Ridge, TN, 37830, USA
[2]Department of Materials Science and Chemical Engineering, Stony Brook University, Stony Brook, NY 11794, USA
[*]Corresponding author. *E-mail addresses:* zhongw@ornl.gov

Abstract

Development of high-strength materials often involves introduction of additional strengthening microstructures that also serve as tritium trapping sites. Such additions in fusion material development could degrade the fuel efficiency in fusion reactors and raise radiological concerns. The contribution of individual microstructure features in hydrogen trapping must be evaluated to ensure fuel efficiency and radiological safety. This study explores the mechanistic origins of deuterium trapping in reduced-activation ferritic–martensitic steels and its correlation to mechanical strengthening. A series of model alloys and engineering steels were fabricated and subjected to different heat treatments to control deuterium trapping site density. Deuterium retention was evaluated using D_2 gas charging and thermal desorption spectroscopy, focusing on the role of grain boundary, dislocation, $M_{23}C_6$ precipitates, and TiC precipitates. Multiscale microstructure characterization and synchrotron X-ray diffraction were performed to characterize microstructure, which was correlated to the deuterium retention property. Results show that TiC precipitates exhibit the highest deuterium trapping capacity, followed by $M_{23}C_6$ precipitates. Dislocation and grain boundary demonstrate the lowest and similar efficiencies. The relationship of trapping quantity and mechanical strengthening of these microstructure features was quantified, demonstrating that TiC precipitates offer highest deuterium trapping per unit of mechanical strengthening.

Keywords: Structure–property relationship; Retention; Strengthening; Thermal desorption spectroscopy

1. Introduction

As a critical energy carrier, hydrogen is increasingly significant in applications ranging from fuel cells [1] and hydrogen storage systems [2] to nuclear fusion reactors [3]. Because of its small atomic size, hydrogen diffuses rapidly and is easily trapped within various materials. The interaction of hydrogen with structural materials, particularly steels, poses significant challenges to their mechanical integrity: hydrogen can change the material's fracture toughness and ductility—a phenomenon known as hydrogen embrittlement. The fundamental mechanisms of hydrogen embrittlement are not completely in consensus, and several mechanisms are proposed, including hydrogen-enhanced decohesion, hydrogen-enhanced localized plasticity, and hydrogen-enhanced strain-induced vacancy formation [4, 5, 6]. However, general consensus exists on the significant role of microstructure in hydrogen embrittlement. Diffusible hydrogen is widely accepted to cause embrittlement [6], suggesting that optimizing microstructure to trap hydrogen effectively can reduce the amount of diffusible hydrogen that reaches crack tips, thereby mitigating the embrittlement risk [7]. In fusion reactors, the challenge extends beyond mechanical degradation. Hydrogen isotopes, particularly tritium, pose additional concerns related to fuel efficiency and radiological hazards caused by tritium retention in reactor materials. Hydrogen isotopes—deuterium and tritium—are harnessed for generating fusion energy. The fusion reaction of deuterium and tritium, ^{2}H (^{3}H, n) ^{4}He, generates 17.6 MeV per fusion event, producing a 14.1 MeV neutron and 3.5 MeV helium particle. Fusion materials face extreme operational conditions, including high-energy neutron bombardment, intense heat flux, mechanical loading, and tritium exposure, leading to significant materials challenges [8, 9, 10]. The retention of tritium in plasma-facing components and structural materials must be carefully managed to minimize safety risks and maintain reactor performance. Developing materials that can withstand these extreme conditions while limiting tritium retention is crucial for the success of fusion energy systems. Therefore, understanding the interaction between hydrogen isotopes in fusion materials, along with the role of microstructure in mitigating these effects, is a key focus for advancing the reliability and efficiency of fusion reactors.

Reduced-activation ferritic–martensitic (RAFM) steels are the primary candidates for structural materials in fusion reactors. They are derived from traditional ferritic–martensitic (FM) steels but are subject to stricter compositional control—particularly with respect to minimizing elements that transmute into long-lived radioactive isotopes—in consideration of waste management and long-term environmental safety [11]. Despite their advantages, RAFM steels, such as F82H and Eurofer 97, exhibit reduced creep resistance compared with second-generation FM steels, such as Grade 91, from which they were originally tailored [12]. This limited creep performance restricts their application at higher operational temperatures, driving ongoing research to develop advanced RAFM steels with enhanced thermal creep properties and improved irradiation resistance. Key strategies to achieve these advancements include the introduction of a high density of nanoscale precipitates [13, 14], refinement of grain structure [15, 16], and optimization of dislocation structures using thermomechanical treatments [17, 18]. These improvements are essential for extending the operational limits of RAFM steels and potentially making them more suitable for the extreme conditions of fusion environments.

While these microstructural modification strengthen the material, they also introduce additional tritium trapping sites. This increased trapping not only affect fuel efficiency but also raise significant safety concerns during reactor maintenance. Previous studies have compared hydrogen retention in various fusion structural materials, including FM steels and oxide dispersion-strengthened (ODS) alloys, generally revealing higher levels of hydrogen retention in stronger materials [19, 20]. However, a fundamental understanding of the mechanisms behind hydrogen trapping in RAFM steels remains inadequate. Specifically, the relationship between microstructural features and their respective roles in hydrogen trapping and mechanical strengthening needs further investigation.

Hydrogen trapping at different microstructural features has been studied across various material systems. Precipitates are widely regarded as strong hydrogen traps and have been explored as a strategy to mitigate hydrogen embrittlement by sequestering hydrogen away from crack tips [7]. In ferritic steels, Ti-, V-, and Nb-rich carbide and nitride are commonly engineered to increase mechanical strength, and they also exhibit strong hydrogen-trapping capabilities. First-principle calculations suggest that both the precipitate/matrix interface and carbon vacancies within the precipitate serve as effective hydrogen traps [21]. Atom probe tomography (APT) has confirmed hydrogen trapping at these interfaces [22, 23, 24]. While hydrogen trapping within vanadium carbide has been reported [25], it is suggested that Mo addition and insufficient annealing increase vacancy concentration, facilitating interior trapping [7]. Scanning Kelvin Probe Force Microscopy further supports hydrogen trapping at TiC interfaces [26]. Prior studies also indicate that hydrogen trapping depends on precipitate interface coherency [27], with higher activation energy associated with incoherent interface, and lowest energy for coherent interfaces [7, 27, 28, 29, 30]

Beyond precipitates, direct observation of deuterium trapping at dislocations and grain boundaries remains challenging, as these features lack significant compositional contrast for APT investigation. Monte Carlo simulations indicate that hydrogen concentrates along dislocations and interacts strongly with dislocation cores, with binding energy maxima aligning with peak hydrogen concentrations at approximately 3 Å from the core [31]. Studies suggest that hydrogen trapping by dislocations may be affected by segregation [22, 32], where hydrogen trapping is associated with carbon segregation and carbon-free dislocation exhibit no hydrogen trapping [32]. However, this observation appears to contradict Density functional theory (DFT) calculation on hydrogen trapping at grain boundaries, which suggest that carbon and nitrogen segregation reduces hydrogen trapping [33]. Such a reduction in hydrogen trapping due to grain boundary segregation may help prevent grain boundary decohesion and subsequent pre-mature failure [34]. Additionally, DFT calculations indicate that hydrogen trapping depends on grain boundary angle [33], a finding confirmed by nanoscale secondary ion mass spectroscopy, which has shown hydrogen trapping at high-angle grain boundaries [35].

Most prior studies focus on specific trapping features in isolation, neglecting the concurrent contribution of other hydrogen-trapping features. Engineering alloys contain a variety of microstructural features that serve as hydrogen traps, and a comprehensive understanding of their combined effects is essential for designing hydrogen-resistant materials. This study investigates the hydrogen trapping behaviors of multiple microstructural features in RAFM steels. Specifically, the relationship between hydrogen trapping and mechanical strengthening is examined to elucidate their combined influence on material performance. Given that tritium retention is a critical challenge for the long-term viability of fusion energy, understanding and controlling the interplay between mechanical strength and tritium retention is crucial for developing structural materials with an optimal balance of strength and minimal tritium retention for advancing the efficiency, safety, and sustainability of fusion reactors.

To achieve this, a series of model alloys and engineering steels have been designed and fabricated. These alloys were subjected to different heat treatments to control the density of hydrogen trapping locations. Multiscale microstructures of the materials were characterized by electron backscatter diffraction (EBSD), scanning transmission electron miscopy (STEM), energy dispersive spectroscopy (EDS) and synchrotron X-ray diffraction (XRD) to investigate the grain size, precipitate, and dislocation distribution, all of which serve as hydrogen trapping sites. The fundamental knowledge of the effect of individual microstructure features on hydrogen trapping and its relationship to mechanical strengthening is critical for materials development for applications subject to a hydrogen environment, including fusion reactors.

2. Experimental

Materials

FM steels exhibit a complex structure that effectively traps hydrogen. To determine the origin of the hydrogen trapping, a comprehensive set of FM steels and model alloys with different microstructures were designed and fabricated. Different heat treatments were applied to control the density of individual hydrogen trapping sites. Table 1 summarizes the materials that were investigated in this work, along with their composition and the heat treatment.

Alloys with four different compositions were fabricated, and each alloy was subjected to two different heat treatments. For each composition, alloys that underwent longer annealing are denoted with "-a" at the end of the sample ID.

- Binary model alloys, Fe-9%Cr, were fabricated as the simplest model alloys. No precipitates were designed in the binary model alloys. Both heat treatments led to recrystallization with different grain size.
- Ternary model alloys, Fe-9%Cr-0.1%C, were fabricated. The added 0.1% carbon led to formation of tempered martensite grain structure and $M_{23}C_6$ precipitates (M=Cr in Fe-9%Cr-0.1%C), which are commonly observed in 9% Cr steel materials. Two different heat treatments were applied, and Sample 9Cr-0.1C-a was subjected to a longer tempering time, resulting in coarser microstructure features and fewer trapping sites.
- Two engineering steels (identified as 9Cr-1TiW-0.1C and 9Cr-1TiW-0.05C) were designed and fabricated, with similar alloying compositions, differing only in carbon content. The 9Cr-1TiW-0.1C alloy contains 0.1% carbon, which led to the formation of both TiC and $M_{23}C_6$ precipitates (M is primarily Cr in engineering steels). By contrast, 9Cr-1TiW-0.05C, with 0.05% carbon, was designed to form only TiC precipitates. Heat treatments for these two alloys were designed based on their phase diagram (Figure 1), ensuring that TiC phase fractions were similar in both alloys and that no $M_{23}C_6$ precipitates formed in 9Cr-1TiW-0.05C. Thermal aging was performed on Samples 9Cr-1TiW-0.1C and 9Cr-1TiW-0.05C to reduce the trapping density to identify the effect of the individual trapping microstructure on hydrogen trapping. The aging temperature was set at 775 °C, at which point no phase transformation or additional phase formation (such as Laves phase or α′) are expected.

Table 1. Summary of materials and their composition (in wt %) and heat treatments.

Sample ID	Compositions	Heat treatment
9Cr	Fe-9Cr	Anneal at 825 °C for 1 h, cold rolling to 90% thickness reduction, and annealing at 825 °C for 0.5 h
9Cr-a		Anneal at 825 °C for 1 h, cold rolling to 70% thickness reduction, and annealing at 825 °C for 6 h
9Cr-0.1C	Fe-9Cr-0.1C	Normalization at 1100 °C for 10 min followed by water quench (WQ), and then temper at 750 °C for 0.5 h followed by air cool (AC)
9Cr-0.1C-a		Thermal aging at 750 °C for 5.5 h on 9Cr-0.1C
9Cr-1TiW-0.1C	Fe-8.7Cr-0.5Mn-0.14Si-0.09Ta-0.14Ti-0.05V-1.0W-0.1C	Normalization at 1120 °C for 1 h, hot rolling at 1100 °C to 70% thickness reduction followed by WQ and temper at 750 °C for 0.5 h followed by AC
9Cr-1TiW-0.1C-a		Thermal aging at 775 °C for 1100 h on 9Cr-1TiW-0.1C

9Cr-1TiW-0.05C	Fe-8.7Cr-0.5Mn-0.14Si-0.09Ta-0.14Ti-0.05V-1.0W-0.05C	Normalization at 1050 °C for 1 h, hot rolling at 1050 °C to 70% thickness reduction followed by WQ, and then temper at 750 °C for 0.5 h followed by AC
9Cr-1TiW-0.05C-a		Thermal aging at 775 °C for 1100 h on 9Cr-1TiW-0.05C

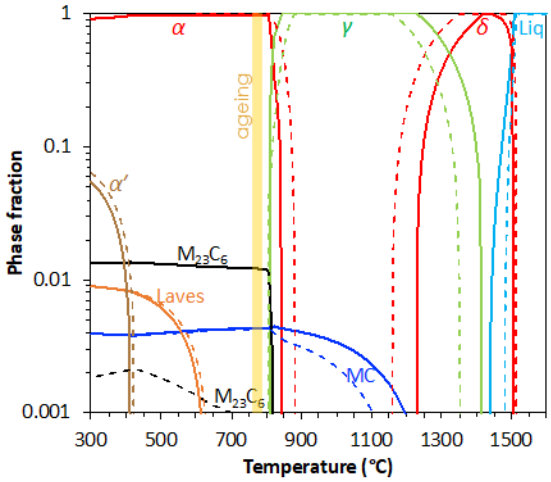

Figure 1. Equilibrium phase diagram for 9Cr-1TiW-0.1C (solid) and 9Cr-1TiW-0.05C (dashed), used for heat-treatment guidance.

Microstructure characterization

The microstructures of these alloys were characterized using EBSD, STEM, EDS, and synchrotron XRD. For EBSD, the scanning steps were 0.5 µm, and the scanning region was 500 × 400 µm. For detailed examination of grain structure and precipitates, a Talos F200X S/TEM equipped with Super-X EDS was utilized. The Super-X EDS system, with its four silicon drift detectors, enabled high-resolution chemical mapping, which was particularly useful for examining the distribution of fine precipitates. To improve the statistical analysis of fine precipitate (below ~10 nm), Thermo Scientific Maps software was used to acquire 20 or more high-resolution EDS maps over a large area for 9Cr-1TiW-0.1C and 9Cr-1TiW-0.05C samples.

High-energy XRD measurements were performed at the Pair Distribution Function (PDF) beamline at the National Synchrotron Light Source-II (NSLS-II). All measurements were performed in transmission mode with an energy of 74.47 keV (0.1665 Å) and an amorphous silicon-based 2D panel detector (PerkinElmer) mounted orthogonal to and centered on the beam path. The sample-to-detector distances and tilts of the detector relative to the beam were refined using a LaB_6 NIST standard. All raw 2D patterns were background corrected by subtracting a dark current image. Noticeable artifact regions were masked. The corrected and masked 2D detector images were then radially integrated to obtain 1D powder diffraction patterns. The background-corrected XRD patterns were analyzed using Rietveld and whole powder pattern modeling (WPPM) macros [36, 37] in TOPAS Academic (BRUKER). The instrument contribution to the broadening of the measured profiles was quantified by fitting the LaB_6 powder NIST standard through modified Thompson–Cox–Hastings pseudo-Voigt (TCHZ) function, with known crystalline-domain size and negligible strain contribution. The lattice parameters, coherent scattering size, and microstrain were quantified via standard Rietveld refinements [36, 38]. The lattice parameters and coherent scattering size obtained from the Rietveld refinement were employed and fixed for each Warren–Averbach analysis [39, 40, 41] to reduce the number of free parameters during the analysis and increase the accuracy of dislocation characterization

Deuterium retention property measurement

A custom-built thermal desorption spectroscopy (TDS) system was used to characterize hydrogen retention. Detailed information of the TDS system is provided elsewhere [19]. This work used D_2 gas to avoid handling radioactive tritium gas. The D_2 gas has significantly lower background than hydrogen gas, thereby improving the measurement sensitivity. Specimens were charged with D_2 gas at 450 °C for 1 h under 760 Torr. After charging, samples remained in the D_2 gas–filled chamber to cool from 450 °C to below 100 °C (< 5min). The D_2 gas was then evacuated, and the specimens were promptly transferred to the thermal desorption spectroscopy (TDS) system. The system was pumped to the vacuum level on the order of 10^{-8} Torr before starting TDS measurement. Typical lag time between the finish of D_2 charging and the start of the TDS experiment is 1 h. During the TDS experiment, the temperature was increased at a rate of 0.5 °C/s, and the desorbed D_2 signal was measured using the Pfeiffer PrismaPlus QME-220 Spectrometer, which was calibrated using the standard D_2 leak from Vacuum Technology Inc. The deuterium diffusivity measured in various FM steels [19] yields a diffusion distance of 12.7±2.0 mm under the D_2 charging condition in this study (450 °C, 1h). This distance was estimated by $2\sqrt{Dt}$, where the D is the diffusivity at 450 °C, and t is D_2 charging time (1 h), and a factor of 2 accounts for hydrogen absorption from both side of samples. Because this diffusion distance far exceeds the sample thickness of 1 mm, deuterium trapping within the sample is in equilibrium with the D_2 environment.

Hardness measurement

Vickers hardness was measured on polished samples using a 0.5 kg load with a 10 s dwell time at room temperature. Each sample underwent 10 measurements, and the average hardness and the standard deviation are reported.

3. Results

Section 3.1 details the microstructure results, including grain structure and precipitates, of investigated samples, and Section 3.2 examines their dislocation. The results of Section 3.1 and Section 3.2 are used to evaluate the density of different hydrogen trapping sites. Section 3.3 presents the thermal desorption spectroscopy results on these samples, and the correlation of hydrogen trapping to microstructure and to mechanical hardness is presented in the discussion in Section 4.

3.1 Multiscale microstructure

The grain structure of the investigated materials is shown in *Figure 2*. These samples fall into two categories: equiaxed grain structure and tempered martensite grain structure. Typically, materials with alloyed carbon contents exhibit tempered martensite grain structure (including 9Cr-0.1C, 9Cr-0.1C-a, 9Cr-1TiW-0.05C, 9Cr-1TiW-0.1C, 9Cr-1TiW-0.1C-a), which is common for carbon-containing steels [42]. By contrast, binary alloys such as Fe-9%Cr exhibit equiaxed grain structure. In addition, thermal aging for 1100 h at 775 °C significantly changes the grain structure of 9Cr-1TiW-0.05C, resulting in a large equiaxed grain structure after prolonged aging (*Figure 2f*).

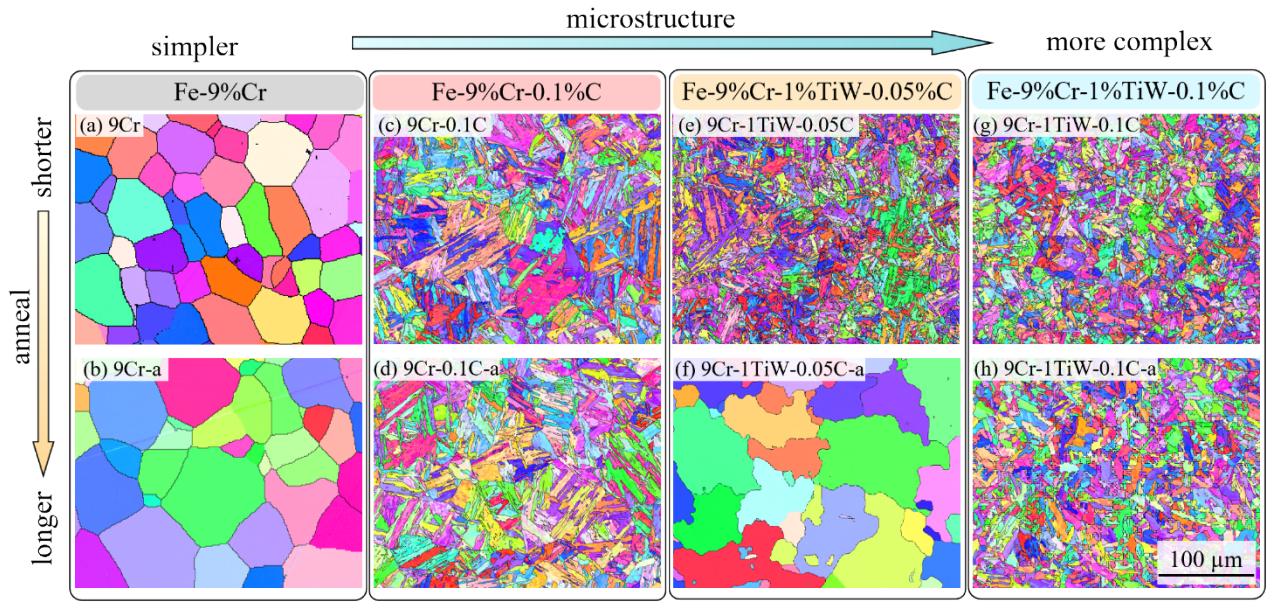

Figure 2. Grain structure of (a-b) binary Fe-9%Cr, (c-d) ternary Fe-9%Cr-0.1%C, engineering steels (e-f) Fe-9%Cr-1%TiW-0.05%C and (g-h) Fe-9%Cr-1%TiW-0.1%C with different heat treatment. Scale bars are the same for all images.

Precipitates play a crucial role in hydrogen trapping. To visualize the distribution of these precipitates, STEM/EDS technique was used to identify the precipitate type, size, and number density, as shown in Figure 3. In binary model alloys, a single phase of ferritic matrix is expected with no designed precipitate. For both heat treatments, the only precipitates observed in the Fe-9%Cr-0.1%C samples were $M_{23}C_6$ precipitates, and the $M_{23}C_6$ precipitates were distributed along the boundary. The $Cr_{23}C_6$ precipitates are smaller in the 9Cr-0.1C: they have an average size of 63 ± 26 nm and a number density of 5.6×10^{19} m^{-3}, as summarized in Table 2. These $M_{23}C_6$ precipitates coarsen significantly after the additional annealing at 750 °C. The precipitates grew larger and elongated along lath boundaries, whereas larger blocky precipitates appeared at tri-junctions of boundaries. In the 9Cr-0.1C-a sample, the average size of $M_{23}C_6$ precipitates increased to 163 ± 113 nm, corresponding to a growth rate of approximately 160%.

The only precipitates observed in the Fe-9%Cr-1%TiW-0.05%C sample were TiC precipitates. Large spherical TiC precipitates were distributed throughout the matrix and had an average size of 67 ± 17 nm in 9Cr-1TiW-0.05C. After 1100 h of annealing at 775 °C, the size of these TiC precipitates remained stable, increasing only slightly to 72 ± 35 nm—a growth of about 7%. This result indicates that TiC precipitates are significantly more stable than $M_{23}C_6$ precipitates, despite the slightly higher annealing temperature and much longer annealing for the 9Cr-1TiW-0.05C-a sample compared with 9Cr-0.1C-a. The higher stability of MX precipitates over $M_{23}C_6$ precipitates has also been reported in other studies [43]. In addition to the coarse TiC precipitates, fine TiC precipitates were also present in 9Cr-1TiW-0.05C, as shown in Figure 4a. The coarse TiC precipitates likely form at the normalization step during the heat treatment, whereas the fine TiC precipitates form during tempering. The visualization of fine TiC precipitates requires high magnification (in this case, ~400,000× magnification). To obtain good statistics of the size distribution of such fine precipitates, 25 partly overlapping high-magnification EDS maps were acquired using the MAPS software; the stitched Ti maps are shown in Figure 4a. Figure 4c shows the size distribution of fine TiC precipitates, which have an average size of 8.3 ± 3.8 nm. Although some TiC precipitates were observed at boundaries and appeared larger, the majority were located within the matrix. For simplicity, all TiC

precipitates were categorized into two groups: coarse TiC precipitates, with an average size of 67 ± 17 nm, and fine precipitates, with an average size of 8.3 ± 3.8 nm. After annealing at 775 °C, these fine TiC precipitates were no longer observed in 9Cr-1TiW-0.05C-a, indicating that finer precipitates are more susceptible to dissolution or coarsening during prolonged heat treatment.

Both TiC and $M_{23}C_6$ precipitates are observed in Fe-9%Cr-1%TiW-0.1%C, as shown in Figure 3e and f. Like in the Fe-9%Cr-0.1%C and Fe-9%Cr-1%TiW-0.05%C samples, $M_{23}C_6$ precipitates were located at the boundary, whereas coarse TiC precipitates were distributed in the matrix. The average sizes for $M_{23}C_6$ and coarse TiC precipitates were 70 ± 27 nm and 88 ± 48 nm, respectively. Similarly, fine TiC precipitates were observed in 9Cr-1TiW-0.1C, as illustrated by the stitched EDS maps in Figure 4b. Unlike in 9Cr-1TiW-0.05C, the fine TiC precipitates were mostly distributed at boundaries in 9Cr-1TiW-0.1C. The mechanism leading to different distribution of fine TiC precipitates in alloys of different carbon contents is not clear and requires further investigation.

Figure 4c shows the size distribution of fine TiC precipitates (diamond symbols) for both 9Cr-1TiW-0.1C and 9Cr-1TiW-0.05C, binned in 0.2 nm intervals. The frequency distribution (in arbitrary units) is plotted as curves to illustrate the trend. The average size and standard deviation of these precipitates are also included. Likely due to their distribution at boundary, and because faster diffusion along the grain boundary facilitates growth, slightly larger TiC precipitates were observed in 9Cr-1TiW-0.1C (10.7 ± 5.3 nm) than in 9Cr-1TiW-0.05C (8.3 ± 3.8 nm). After the thermal annealing at 775 °C, fine TiC precipitates were no longer observed, similar to what was seen in 9Cr-1TiW-0.05C-a. The average size of precipitates increased to 308 ± 198 nm for $M_{23}C_6$ and 96 ± 43 mm for TiC, representing growth ratios of 338% and 9%, respectively. This consistent TiC growth rate in both Fe-9%Cr-1%TiW-0.1%C and Fe-9%Cr-1%TiW-0.05%C further underscores the higher stability of TiC precipitates compared with $M_{23}C_6$ precipitates. No other precipitates were observed after thermal annealing in neither Fe-9%Cr-1%TiW-0.1%C nor Fe-9%Cr-1%TiW-0.05%C, in agreement with the thermodynamics calculation, shown in Figure 1.

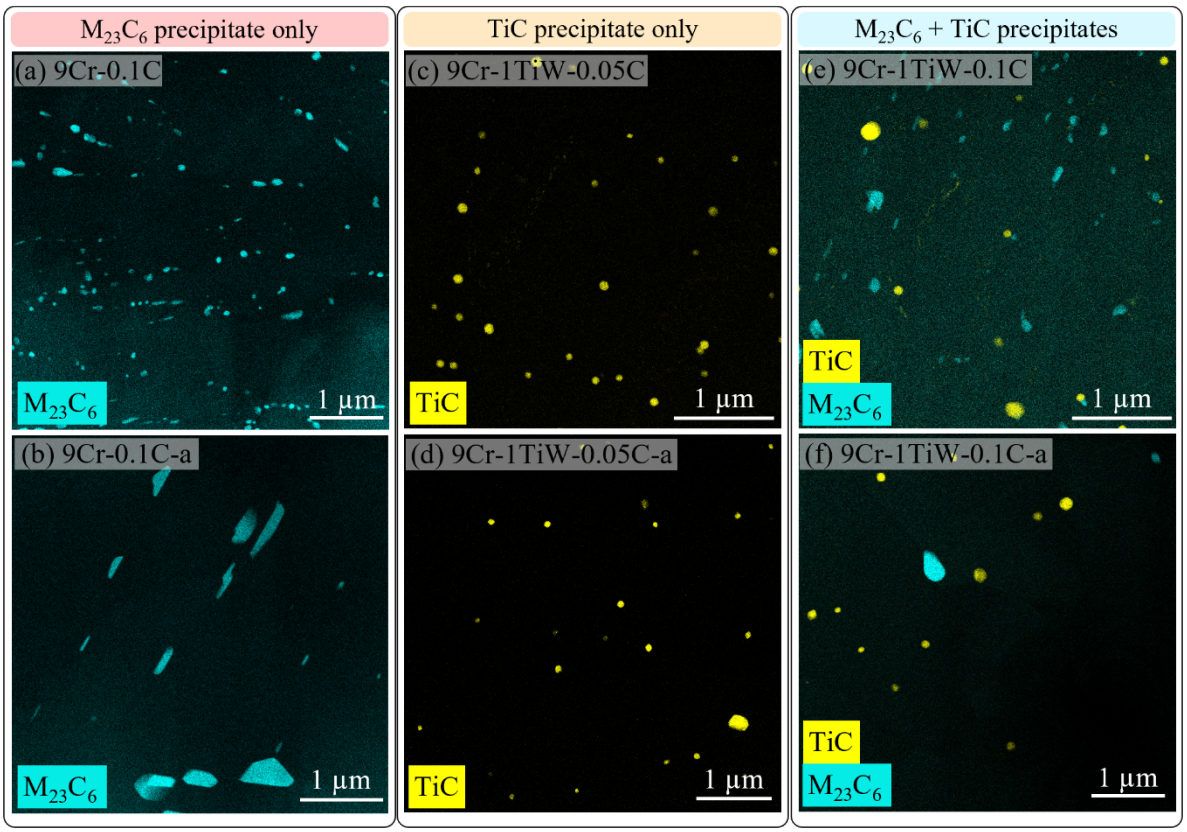

Figure 3. STEM/EDS maps showing the distirbution of TiC and $M_{23}C_6$ precipitates in (a) 9Cr-0.1C and (b) 9Cr-0.1C-a, which contain only $M_{23}C_6$ preciptiates; (c) 9Cr-1TiW-0.05C and (d) 9Cr-1TiW-0.05C-a, which contain only TiC precipitates; and (e) 9Cr-1TiW-0.1C and (f) 9Cr-1TiW-0.1C-a, which contain both $M_{23}C_6$ and TiC precipitates.

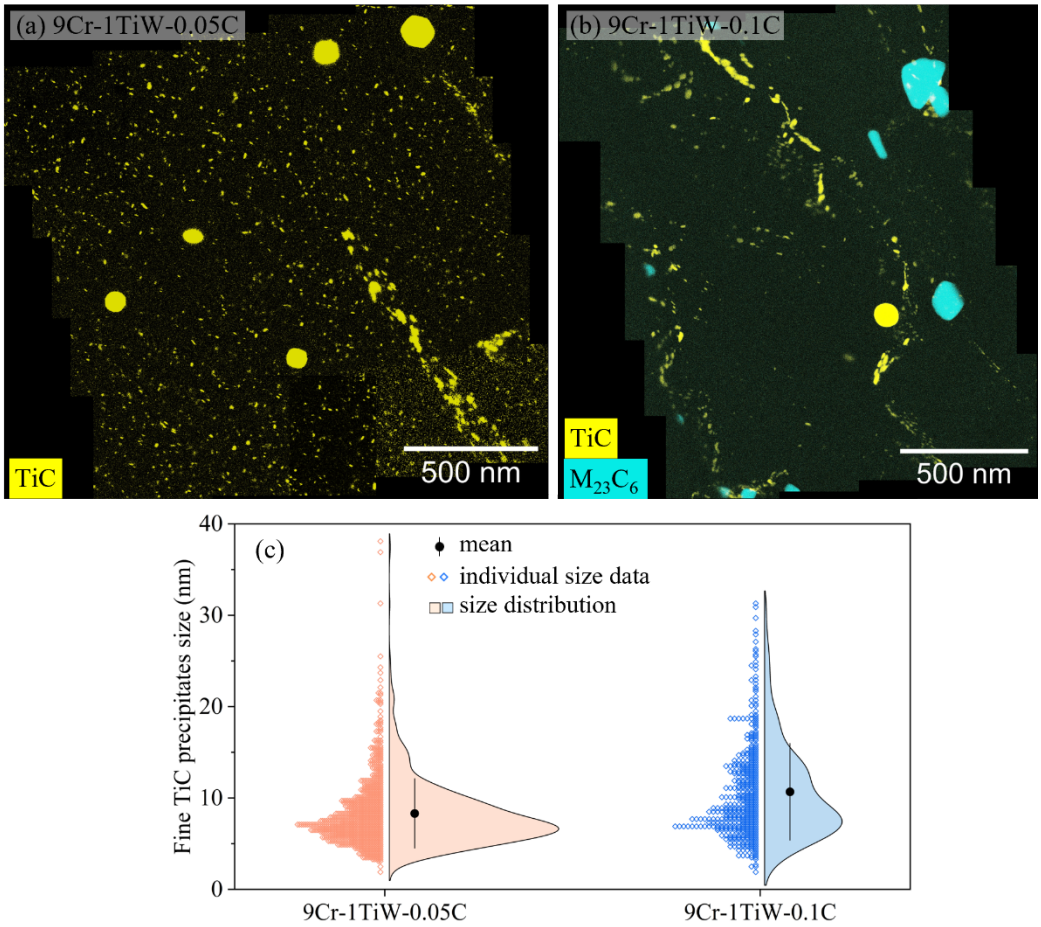

Figure 4. Stitched Ti or Ti/Cr EDS maps in (a) 9Cr-1TiW-0.05C and (b) 9Cr-1TiW-0.1C to show the distribution of fine TiC preciptiates, and (c) individual size data of TiC precipitates, binned in 0.2 nm interval, along with their size frequency distribution, mean, and standard deviation. The size frequency distribution are plotted in arbitrary unit in x-axis.

3.2 Dislocation density quantification

Dislocations were present in investigated samples, and their density varied depending on the applied heat treatment. The integrated X-ray spectra for 9Cr-0.1C, 9Cr-0.1C-a, 9Cr-1TiW-0.05C, 9Cr-1TiW-0.1C, and 9Cr-1TiW-0.1C-a are shown in Figure 5. The dominant peaks are attributed to the matrix, whereas the minor peaks are attributed to the $M_{23}C_6$ and TiC precipitates. For coarse grain samples (9Cr, 9Cr-a and 9Cr-1TiW-0.05C-a), their 2D patterns do not show a full ring because of the limited number of grains that were measured by the X-ray beams. Therefore, only the samples with tempered martensite grain structure were used for dislocation density calculations. The dislocation density affects the peak broadening in XRD: narrower peaks represent lower dislocation densities. An example of diffraction pattern of {110} planes of the matrix for 9Cr-1TiW-0.1C and aged 9Cr-1TiW-0.1C-a is shown in the Appendix, Figure A.1a. Narrower full width at half maximum (FWHM) were observed after the thermal aging (in 9Cr-1TiW-0.1C-a), partly owing to the dislocation recovery from the thermal aging. On-zone STEM was used to image the dislocation networks, as shown in the Appendix, Figure A.1b and Figure A.1c. Sample 9Cr-1TiW-0.1C exhibited a high density of dislocation networks; dislocation was significantly reduced after thermal aging, and only isolated dislocation segments were observed in aged 9Cr-1TiW-0.1C-a.

To quantify the dislocation density, a standard method to separate size and strain broadening using Fourier coefficients of multiple orders of reflection is known as the Warren–Averbach method [41]. In this method, the XRD peak intensities are represented as a Fourier sum:

$$A_{hkl}(L) = A^S_{hkl}(L)A^D_{hkl}(L) = A^S_{hkl}\exp\left[\left(-\frac{2\pi^2L^2}{d^2_{hkl}}\right)\langle\varepsilon^2_{hkl}(L)\rangle\right] \#(1)$$

where $A_{hkl}(L)$ is the real part of the Fourier coefficient, A^S_{hkl} is the coherent scattering size-broadening contribution, L is the length in the real space, and d^2_{hkl} is the interplanar distance. According to Wilkens [44], the microstrain component to the peak broadening in the Warren–Averbach analysis $\langle\varepsilon^2_{hkl}(L)\rangle$ can be written as follows:

$$\langle\varepsilon^2_{hkl}(L)\rangle = \frac{\rho b^2}{4\pi}\overline{C}_{hkl}f^*\left(\frac{L}{R_e}\right) \#(2)$$

where $f^*(L/R_e)$ is the Wilkens function that provides the appropriate decay to the Fourier transform for increasing L, ρ is the dislocation density, b is the Burgers vector, R_e is the outer cutoff radius of the dislocation strain field, and $\overline{C}_{hkl}$ is the *hkl*-dependent average dislocation contrast factor. The value $\overline{C}_{hkl}$ can be averaged over the *hkl* multiplicity of the *hkl*-type reflections and the average contrast factor for cubic crystals is given by Eq. (3) [45, 46]:

$$\overline{C} = \overline{C}_{h00}\left(1 - qH^2\right) \#(3)$$

where $\overline{C}_{h00}$ is the average contrast factor corresponding to the *h00* reflection, and q is a parameter that depends on the character of dislocation and the elastic constant. The value H is represented as follows:

$$H^2 = \frac{h^2k^2 + h^2l^2 + k^2l^2}{(h^2 + k^2 + l^2)^2} \#(4)$$

where *h, k,* and *l* are the Miller indices of each peak. The value of $\overline{C}_{h00}$ and q are determined using elastic constants C_{11} = 237 GPa, C_{12} = 141 GPa, and C_{44} = 116 GPa [47] along with Eqs. (5–7) [48]:

$$\overline{C}_{h00} = a\left[1 - \exp\left(-{}^{A_i}/_{b}\right)\right] + cA_i + d \#(5)$$

$$q = a'\left[1 - \exp\left(-{}^{A_i}/_{b'}\right)\right] + c'^{A_i} + d' \#(6)$$

$$A_i = {}^{2c_{44}}/_{(c_{11} - c_{12})} \#(7)$$

where *a, b, c, d, a′, b′, c′,* and *d′* depend on the dislocation type and constant value of C_{12}/C_{44}. The calculated dislocation density is provided in Table 2. For recrystallized and coarse grain samples (9Cr, 9Cr-a, and 9Cr-1TiW-0.05C-a), the dislocation densities are very low, and they cannot be quantified using the same method because of the limited sampling grains. Therefore, a low dislocation density of 1×10^{10} m^{-2} was applied to these samples, which is several orders of magnitude lower than for other samples.

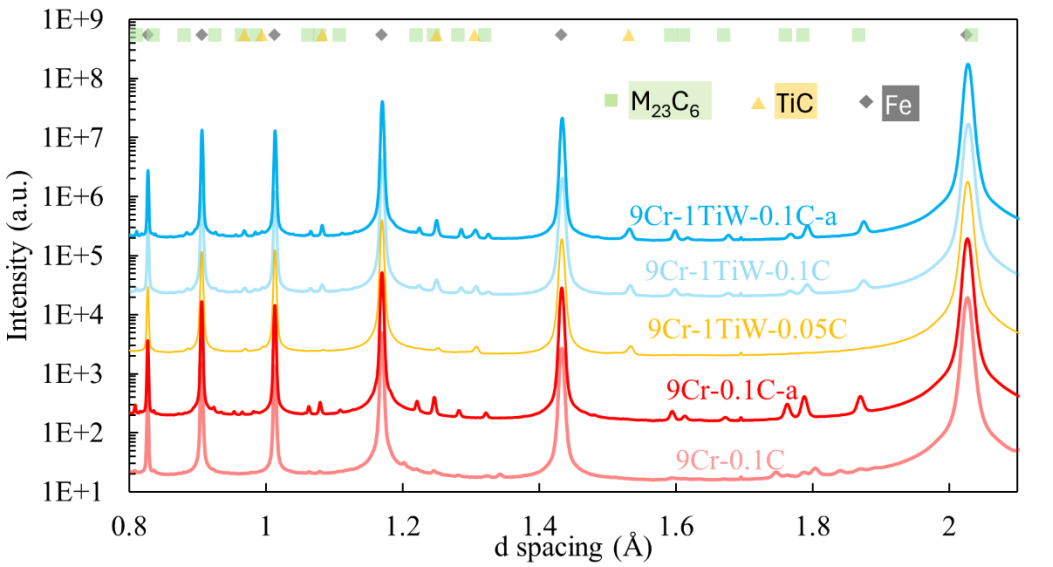

Figure 5. Integrated X-ray intensity spectra for 9Cr-0.1C, 9Cr-0.1C-a, 9Cr-1TiW-0.05C, 9Cr-1TiW-0.1C, and 9Cr-1TiW-0.1C-a.

3.3 Deuterium retention

The investigated samples underwent D_2 gas charging at 450 °C for 1 h, followed immediately by TDS measurement. Figure 6a and b present the deuterium desorption profiles as a function of temperature; Figure 6b highlights the lower desorption flux. Multiple desorption peaks were observed for each sample, corresponding to deuterium de-trapping scenarios at various temperatures. Cumulative desorption profiles are shown in Figure 6c and d; Figure 6d highlight the low cumulative desorption.

In general, 9Cr-1TiW-0.1C and 9Cr-1TiW-0.05C exhibit the largest amount of deuterium trapping, followed by their aged counterparts, 9Cr-1TiW-0.1C-a and 9Cr-1TiW-0.05C-a. Binary Fe-9%Cr and ternary Fe-9%Cr-0.1%C alloys exhibit less deuterium trapping. TDS shows deuterium desorption occurred at low temperature (~100–300 °C) or high temperature (~400–800 °C). At high temperatures, deuterium desorption is relatively more significant, illustrated by the steeper slopes in Figure 6c and d.

To identify the deuterium trapping origin and to understand the microstructure effect on deuterium retention, correlation of deuterium retention and the materials microstructure must be performed. First, the Fe-9%Cr alloys (the simplest microstructure) exhibit the lowest deuterium retention. The two binary alloys (9Cr and 9Cr-a) exhibit large equiaxed grain structure, with practically no dislocation or designed precipitate. Small humps at ~500–800 °C are observed in 9Cr and 9Cr-a. These humps have similar shape and intensity, indicating that the desorption is due to the same trapping mechanism. Grain boundaries are present in the 9Cr and 9Cr-a samples, but deuterium desorption at temperatures of ~500–800 °C is likely not attributable to grain boundaries. As detailed later in this section, deuterium de-trapping from grain boundaries occurs at lower temperatures (less than about 300 °C), and low areal density of boundary ($<3 \times 10^4$ m^{-1}) from the coarse grain structure has negligible effects on deuterium retention. In addition, the grain boundary density in 9Cr is about 40% higher than in 9Cr-a, whereas the amount of desorbed deuterium is similar for both alloys, further supporting the finding that the deuterium desorption at ~500–800 °C is not attributable to grain boundary trapping.

Deuterium desorption at ~500–800 °C in 9Cr and 9Cr-a is attributed to the coarse oxide particles. A low number density of coarse oxide particles was observed in the 9Cr samples, as shown in a representative

backscattered electron image in Appendix Figure A.2a). The EDS spectra in Appendix Figure A.2c support the identification of these particles as oxide. Although no second-phase particles are expected in a pure binary Fe-9%Cr system, the observed coarse oxide particles likely originate from impurities introduced during processing. However, these coarse oxide particles were not observed in the ternary model alloys or engineering steels in this study. A representative backscattered image of 9Cr-0.1C is shown in Appendix, Figure A.2b. The absence of oxide particles in ternary Fe-9%Cr-0.1%C model alloys and engineering steels are attributed to the addition of carbon alloying element. In the binary Fe-9%Cr alloy, oxides likely form during solidification due to the oxygen impurity. However, in carbon-containing alloys, carbon reacts with oxygen in the melt to form carbon monoxide, effectively removing oxygen and preventing the formation of oxide particles. This is consistent with the observations reported in Ref. [49].Like in the 9Cr-a sample, 9Cr-1TiW-0.05C-a exhibits coarse grain structures as well as very low dislocation density. Both 9Cr-a and 9Cr-1TiW-0.05C-a show no deuterium desorption at low temperature (<400 °C), indicating the lack of deuterium trapping features with low de-trapping energy for these two samples. Sample 9Cr-1TiW-0.05C-a shows large amount of deuterium desorption (~0.2 mol D_2/m^3) at high temperature (>400 °C), which is attributed to TiC precipitates, the only dominant microstructure features in 9Cr-1TiW-0.05C-a. This observation clearly indicates that the significant deuterium de-trapping from TiC precipitates, which occurs at temperatures greater than 400 °C.

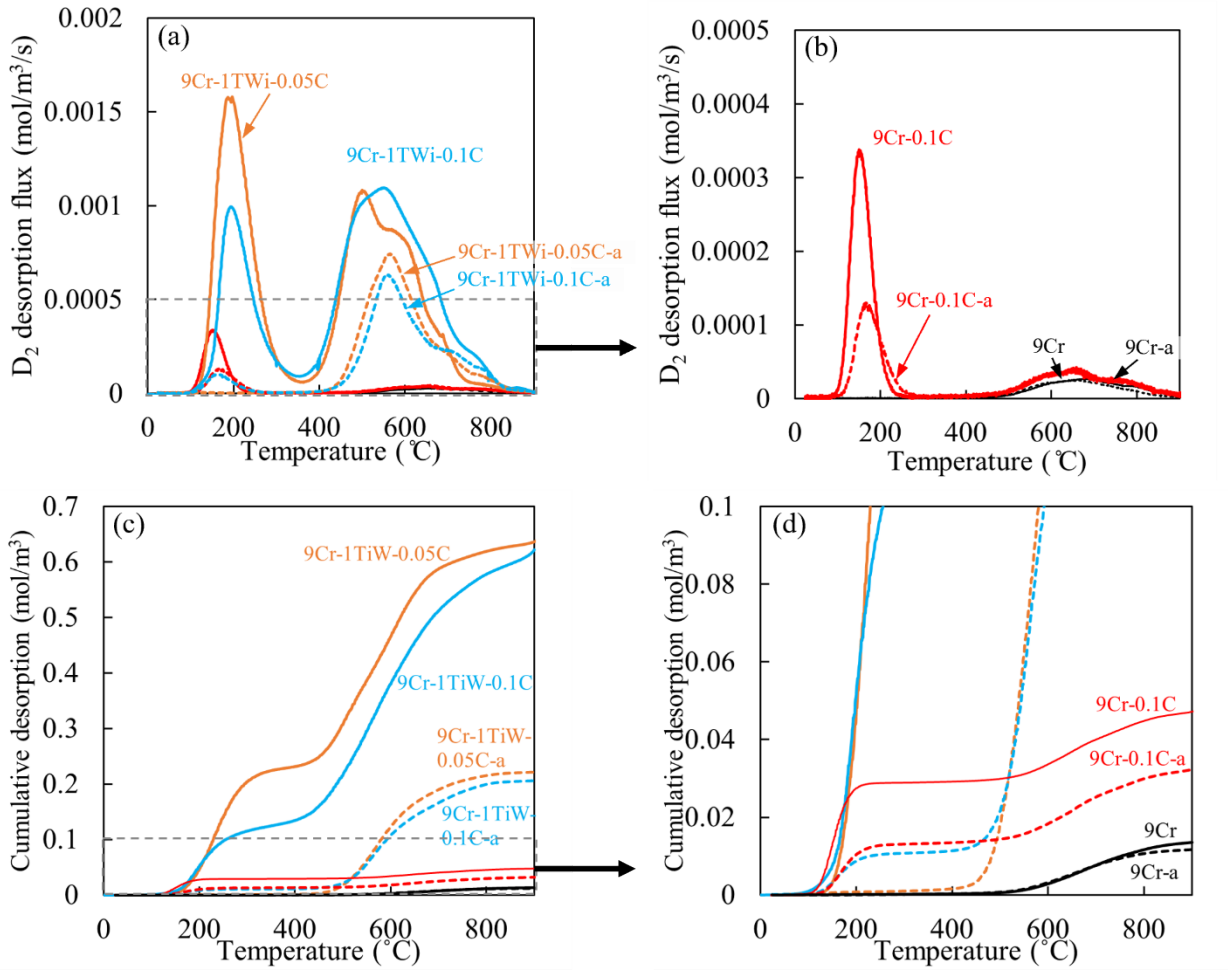

Figure 6. Desorption profiles up to 900 °C. (a, b) Deuterium desorption profiles and (c, d) cumulative desorption profiles.

The low-temperature desorption peak at ~100–300 °C was observed on multiple samples, including both ternary alloy Fe-9%Cr-0.1%C and high-carbon steel Fe-9%Cr-1%TiW-0.1%C. This peak was also observed in as-received 9Cr-1TiW-0.05C but not in the aged 9Cr-1TiW-0.05C-a. Correlating to the microstructure of these samples, all samples that exhibit low temperature deuterium desorption have dislocation and lath martensite grain structure, indicating that deuterium desorption at ~100–300 °C is attributed to deuterium de-trapping from dislocation and lath martensite grain boundary. This correlation is further supported by the deuterium desorption comparison of 9Cr-1TiW-0.05C with 9Cr-1TiW-0.05C-a. Low-temperature (~100–300 °C) deuterium desorption occurs in 9Cr-1TiW-0.05C but not in 9Cr-1TiW-0.05C-a because of the loss of the lath martensite grain structure and dislocation recovery in 9Cr-1TiW-0.05C-a. Therefore, low temperature desorption is attributable to dislocations and lath martensite grain boundaries.

Analysis of the low-temperature desorption profile shows that the low-temperature "peak" exhibits an asymmetric shape that cannot fit well using a single Gaussian peak, as shown in Figure 7a for 9Cr-1TiW-0.05C. A Gaussian distribution of deuterium desorption has been commonly observed and used for fitting thermal desorption profiles and is expected for deuterium de-trapping from a single trapping site [50, 51, 52]. The low-temperature desorption for 9Cr-1TiW-0.05C cannot achieve a good fitting using a single Gaussian peak (Figure 7a), but can achieve a good fitting using two Gaussian peaks (Figure 7b), indicating that the low-temperature desorption is attributed to two trapping mechanisms with similar de-trapping temperatures. This result is in contrast to the desorption profile for the quenched binary Fe-9%Cr, which was obtained by heating 9Cr-a to 1100 °C for 60 min, followed by water quench, and subsequently tempered for 10 min at 720 °C. The quenched binary Fe-9%Cr does not exhibit lath martensite grain structure because it lacks the carbon required for lath martensite grain structure formation; its grain structure is shown in Figure 7e. Quenched Fe-9%Cr contains dislocations, and the thermal desorption profile of Fe-9%Cr exhibits a single deuterium desorption peak that can be fitted with a single Gaussian peak, as shown by the low-temperature desorption profile in Figure 7c. Such a contrasting observation demonstrates that the low-temperature desorption for the Fe-9%Cr-0.1%C, Fe-9%Cr-1%TiW-0.1%C, and as-received Fe-9%Cr-1%TiW-0.05%C is attributable to both dislocation and grain boundary (mostly lath boundary).

Lath boundaries are the dominant boundary type in the tempered martensite grain structure, which mostly has misorientation angle less than approximately 10° between neighboring laths [42]. Lath boundaries can be considered as an array of dislocations [53]; thus the deuterium de-trapping temperature from grain boundary and dislocation are only slightly different.

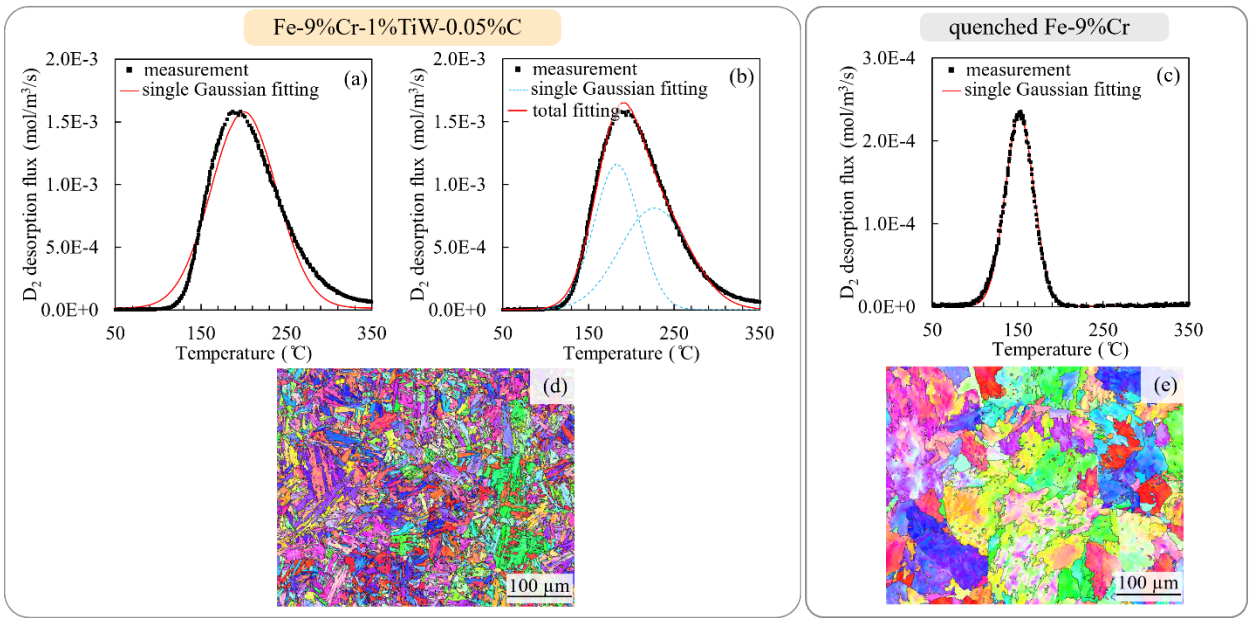

Figure 7. Low-temperature desorption flux in as-received Fe-9%Cr-1%TiW-0.05%C (a) fit with a single Gaussian peak, (b)fit with two Gaussian peaks, and (c) low-temperature desorption flux in quenched Fe-9%Cr fit with a single Gaussian peak. The grain structures of (d) Fe-9%Cr-1%TiW-0.05%C (same as Figure 2e) and (e) quenched Fe-9%Cr.

The high-temperature deuterium desorption in 9Cr-0.1C, 9Cr-0.1C-a is attributable to the $M_{23}C_6$ precipitates. However, the amount of deuterium desorption at high temperature is small (<0.02 mol D_2/m^3) for both 9Cr-0.1C and 9Cr-0.1C-a, indicating the low capacity for deuterium trapping by $M_{23}C_6$ precipitates. This result is further illustrated by the comparison of high-carbon steel Fe-9%Cr-1%TiW-0.1%C and low-carbon steel Fe-9%Cr-1%TiW-0.05%C: both alloys exhibit similar total deuterium trapping in as-received and annealed conditions, regardless of additional $M_{23}C_6$ precipitates in Fe-9%Cr-1%TiW-0.1%C.

4. Discussion

Correlation of individual microstructure features to their deuterium trapping

Individual microstructure features contribute differently to deuterium retention; they trap different amounts of deuterium with distinct de-trapping energy. To correlate the individual features to deuterium trapping quantity, the density of individual trapping sites is estimated from the microstructure characterization.

A prior study using atom probe tomography demonstrates that the interfaces are the dominant deuterium trapping sites [22, 23]. This study involved estimating the areal density of different trapping sites, including precipitate boundary, grain boundary, and dislocation. Although both fine and coarse TiC precipitates were observed, TDS experiment showed similar high-temperature desorption positions after thermal aging for 9Cr-1TiW-0.05C and 9Cr-1TiW-0.1C, indicating that deuterium was trapped via the same mechanism in fine TiC precipitates as in coarse TiC precipitates.

Size, number density, and areal interface density of deuterium trapping sites are summarized in Table 2. The areal density of precipitates is calculated as $\rho_{ppt} = \sum_i 4\pi r_i^2 N$, where N is the number density of the precipitates, and r_i is the radius of precipitate i. Tempered martensite generally has hierarchical grain structure with predominant lath boundary [42]. The lath boundary can be visualized using STEM, and boundary areal density is estimated using $\rho_{GB} = L_{GB}/A_{TEM}$, where the L_{GB} is the total length of boundary within the observation area A_{TEM} in a TEM foil. An example of outlined boundary in the STEM image of

9Cr-0.1C-a is shown in the Appendix, Figure A.3. For coarse grain structure (9Cr, 9Cr-a and 9Cr-1TiW-0.05C-a), boundary areal density is estimated from the EBSD analysis using the same formula $\rho_{GB} = L_{GB}/A_{EBSD}$, where L_{GB} is the total length of boundary (>10°) within the scanning area A_{EBSD}. Dislocations are line defects in the crystalline structure, which exhibits strain field around dislocation lines [54]. Similar to the concept of point defect interaction with dislocation [55], the present study considers a cylinder with its axis as the dislocation line that traps deuterium at the cylinder surface. Previous work has utilized grand canonical Monte Carlo simulation to examine the hydrogen interactions with dislocation in α-Fe [31] and found that most hydrogen was trapped within the core radius of dislocation, which was estimated as 5× the Burgers vectors [56]. To compare the deuterium trapping capacity of different microstructure features, the trapping capacity per unit area was calculated based on deuterium retention and the areal density of trapping sites. Trapping capacity is defined as the amount of trapped deuterium per unit area of interface (in the unit of mol/m^2). Using the linear least-squares fitting on the retention and the areal density of trapping sites, the trapping capacity was obtained, as shown in the Table 2. It is important to note that the measured deuterium trapping in Figure 6 is expressed in mol/m^3, representing experimentally measured deuterium retention with respect to sample volume. In contrast, the trapping capability represents deuterium trapping per unit area of interface of an individual interface (mol/m^2), aligning with prior studies that highlight dominant deuterium trapping at interfaces [22, 23]. The results show that TiC precipitates exhibit highest trapping capacity, 6.8×10^{-7} mol/m^2, and the trapping capacity of $M_{23}C_6$ precipitates, dislocation, and boundary are 7.7×10^{-8} mol/m^2, 2.2×10^{-8} mol/m^2, and 2.0×10^{-8} mol/m^2, respectively.

To support the validity of the trapping capacity obtained from linear least-square fitting, the deuterium trapping of individual microstructure features (in unit of mol/ m^3) was calculated by multiplying the trapping capability (in the unit of mol/m^2) by the areal density of each interface type (m^2/m^3), as listed in Table 2). The calculated deuterium trapping was then compared to the experimentally measured deuterium trapping from TDS. Figure 8a presents this comparison for ternary alloys and engineered steels, where black, blue, and red symbols represent total trapping, trapping below 400 °C, and trapping above 400 °C, respectively. The consistency between calculated and measured deuterium trapping, supports the validity of the trapping capacity calculation. Such calculations allow quantification of individual microstructural contribution to total deuterium trapping.

Figure 8b compares the experimentally measured deuterium trapping from TDS (black histogram) with the calculated breakdown by individual microstructure features (colored histogram). The results indicate that TiC precipitates account for the majority of deuterium trapping, whereas $M_{23}C_6$ precipitates contribute only a small fraction. Dislocation and boundary contribute noticeably to deuterium trapping, but they exhibit lower desorption temperature because of their weaker binding energy with deuterium.

Both $M_{23}C_6$ and TiC precipitates are primarily distributed along boundaries in 9Cr-1TiW-0.1C (see Figure 3e and Figure 4b). The presence of precipitates at grain boundaries reduces the “effective” boundary areal density (i.e. boundaries free of precipitates) compared to the total measured boundary areal density. Unlike $M_{23}C_6$ precipitates, which are observable in STEM bright field image (see Appendix Figure A.3), nanoscale TiC precipitates are not directly visible in such images. As a result, the “effective” boundary areal density is lower than the measured values reported in Table 2. This reduced "effective" boundary areal density contributes to a noticeably lower desorption peak at low temperatures in 9Cr-1TiW-0.1C, despite only slight differences in the measured boundary and dislocation areal densities between 9Cr-1TiW-0.1C and 9Cr-1TiW-0.05C. This observation is consistent with the APT finding in Ref. [32], which demonstrates locally reduced deuterium trapping at boundary near precipitates.

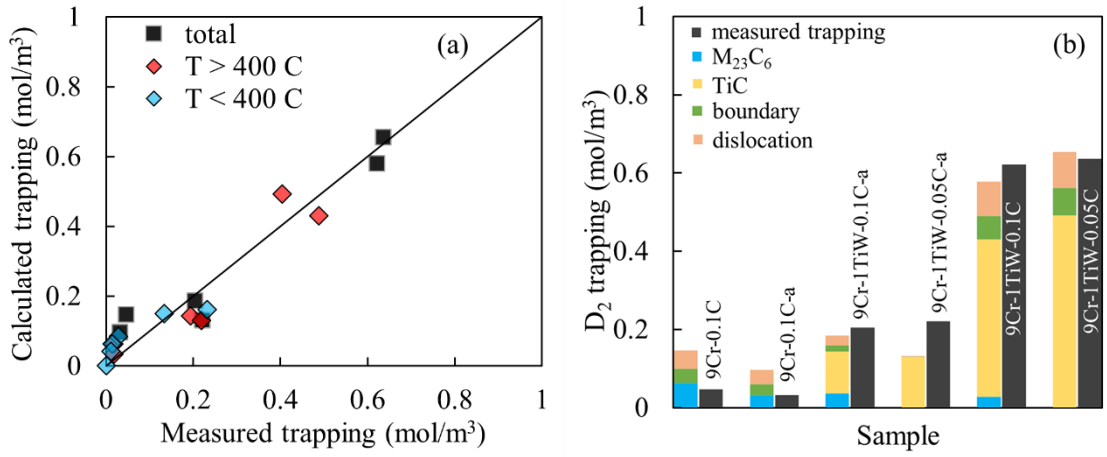

Figure 8. (a) Comparison of calculated and measured deuterium trapping. Black, blue and red symbols represent total, low-temperature (<400 °C), and high-temperature (>400 °C) deuterium trapping. (b) Individual microstructure features contribution to deuterium trapping compared with the total measured deuterium trapping (in black histogram).

Table 2. Summary of size, number density, and areal density of $M_{23}C_6$ precipitate, TiC precipitate, dislocation, and boundary.

Sample	$M_{23}C_6$ precipitate			TiC precipitate			Dislocation		Boundary
	Size (nm)	Number density (m^{-3})	Areal density (m^{-1})	Size (nm)	Number density (m^{-3})	Areal density (m^{-1})	Density (m^{-2})	Areal density (m^{-1})	Areal density (m^{-1})
9Cr	NO†			NO†			1.0×10^{10}	78	2.2×10^{4}
9Cr-a	NO†			NO†			1.0×10^{10}	78	3.0×10^{4}
9Cr-0.1C	63 ± 26	5.6×10^{19}	8.1×10^{5}	NO†			2.8×10^{14}	2.2×10^{6}	1.8×10^{6}
9Cr-0.1C-a	163 ± 113	3.4×10^{18}	4.2×10^{5}	NO†			2.1×10^{14}	1.6×10^{6}	1.4×10^{6}
9Cr-1TiW-0.05C	NO†			67 ± 17 (8.3 ± 3.8)††	1.3×10^{19} (2.0×10^{21})††	2.0×10^{5} (5.2×10^{5})††	5.5×10^{14}	4.3×10^{6}	3.5×10^{6}
9Cr-1TiW-0.05C-a	NO†			72 ± 35	9.5×10^{18}	1.9×10^{5}	1.0×10^{10}	78	2.1×10^{4}
9Cr-1TiW-0.1C	70 ± 27	2.1×10^{19}	3.7×10^{5}	88 ± 48 (10.7 ± 5.3)††	5.6×10^{18} (9.0×10^{20})††	1.8×10^{5} (4.1×10^{5})††	5.3×10^{14}	4.1×10^{6}	3.0×10^{6}
9Cr-1TiW-0.1C-a	308 ± 198	1.2×10^{18}	4.7×10^{5}	96 ± 43	4.5×10^{18}	1.6×10^{5}	1.5×10^{14}	1.2×10^{6}	8.4×10^{5}
Trapping capacity (mol/m^2)	7.7×10^{-8}			6.8×10^{-7}			2.2×10^{-8}		2.0×10^{-8}

† Not observed

†† The first and second number are for coarse and fine TiC precipitates, respectively.

Correlation of deuterium trapping with mechanical strengthening

Vickers hardness was measured at room temperature for the materials investigated in this work; their averaged hardnesses are listed in Table 3. The hardness results are plotted in Figure 9, showing their relationship with the total amount of deuterium retention. In addition, other FM steels and ODS steels reported elsewhere [19] were included, such as Eurofer 97, castable nanostructured alloys (CNAs) and Grade 92 steels, M4 Fe-9Cr, 14YWT-SM13, and 9YWTV-PM2. The total as-reported deuterium retention

in these alloys [19] was measured in the same way as this work. Although Vickers hardness was not reported for all these alloys, yield strength (YS) was readily reported in the literature [57, 58, 13, 59, 60, 61], and the relationship $YS = -90.7 + 2.876H_V$ was used to estimate the Vickers hardness [62]. It is noted that the deuterium charging was performed at an elevated temperature (450 °C), whereas hardness measurements were performed at room temperature, as room-temperature mechanical property data are more widely available.

Table 3. Average Vickers hardness (HV1) of binary, ternary, and engineering alloys.

Sample	9Cr	9Cr-a	9Cr-0.1C	9Cr-0.1C-a
HV1	88.7 ± 1.7	86.7 ± 1.7	172.6 ± 2.1	146.2 ± 3.8
Sample	9Cr-1TiW-0.05C	9Cr-1TiW-0.05C-a	9Cr-1TiW-0.1C	9Cr-1TiW-0.1C-a
HV1	221.5 ± 3.4	115.8 ± 2.6	203.0 ± 6.9	134.1 ± 3.3

In general, materials with higher strength tend to trap more deuterium, although significant variation exists. ODS steels exhibit both the highest strength and the greatest deuterium trapping. Importantly, some classes of steels demonstrate similar strength but very different levels of deuterium trapping. This observation clearly highlights the distinct roles that individual microstructural features play in deuterium trapping versus mechanical strengthening and motivates detailed analysis of the individual microstructure features to understand their contribution to mechanical strengthening and their correlation with the deuterium trapping properties.

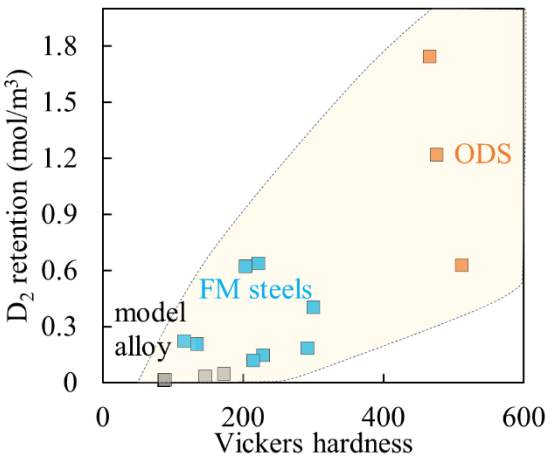

Figure 9. Total deuterium retention (charged at 450 °C) and Vickers hardness at room temperature relation for binary, ternary model alloys, FM steels, and ODS steels, including the data reported elsewhere [19]. The Vickers hardness of ODS and some FM steels are converted from the measured yield strength [57, 58, 13, 59, 60, 61].

The strengthening contribution from individual microstructure features are evaluated using the classic dispersed barrier hardening model [63]. Formula $\Delta\sigma = \alpha M\mu b\sqrt{Nd}$ is used to estimate the strengthening contribution for $M_{23}C_6$ and TiC precipitates, where Taylor factor M is 2.9 for ferritic steels, shear modulus μ is 80.8GPa, Burgers vector b of dislocation is 0.248nm [64], N is the number density of precipitates, d is the size of the precipitates, and the strength factor α (a function of size and shape of the barrier [65]) has a value smaller or equal to 1 [66]. The grain boundary strengthening is estimated based on the morphology of the grain; $M\mu b/\lambda$ and $\beta M\mu b/\sqrt{d_g}$ were used to estimate the tempered martensite structure and the equiaxed grain structure, where λ is lath width for tempered martensite structure, d_g is the grain size of equiaxed grain, and the constant β is estimated as 4380 $m^{-1/2}$ [67]. The strengthening contribution from

dislocation is estimated as $\Delta\sigma = \alpha M \mu b \sqrt{\rho}$, where ρ is the dislocation density. Scattered value of strengthening factor α for dislocation has been reported and used in ferritic steels, ranging from <0.1 to approximately 0.6 [68, 69, 70, 71, 72, 64, 73, 74, 75, 76]. Such wide range of dislocation strength factors is not only due to different composition and processing for steels but also may depend on the method of their derivation. This work used a mean strength factor for dislocation of 0.3, acknowledging that the accurate strengthening factor requires further investigation. The strengthening factors and the strengthening contribution of each feature are summarized in the Appendix, Table A.1.

Figure 10 shows the correlation between deuterium trapping and calculated mechanical strengthening for individual microstructure features in RAFM steels. These microstructure features exhibit different trapping/strengthening relationships. The TiC precipitates demonstrate highest deuterium trapping for the same strengthening levels, followed by $M_{23}C_6$ precipitates, boundary, and dislocation. Although TiC precipitates are the strongest deuterium-trapping features in RAFM steels, they are not necessarily undesirable precipitates in fusion materials. On the contrary, a high number density of precipitates is needed in materials for extreme environments, such as fission and fusion applications, because they contribute to high-temperature creep strength and to irradiation sink strength against defect formation. This work provides valuable insight into the origins of deuterium trapping in RAFM steels and establishes a fundamental correlation between deuterium trapping and mechanical strengthening.

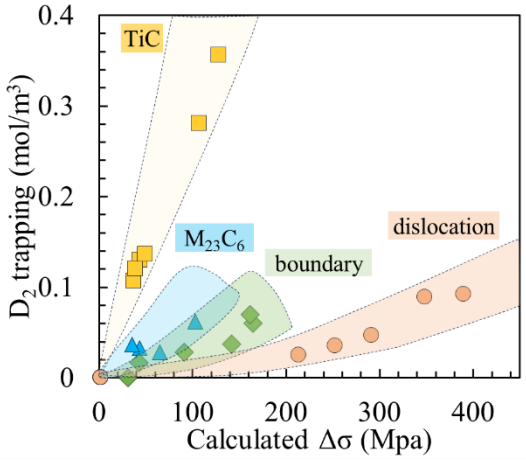

Figure 10. The relationship between deuterium trapping and the strengthening contribution for common strengthening features in RAFM steels: TiC, $M_{23}C_6$, dislocation, and grain boundary.

Effect of D_2 gas charging conditions on trapping

This study specifically investigated deuterium retention and the trapping capacity of individual microstructural features under D_2 gas charging condition at 450 ˚C and 760 Torr. The effect on gas charging condition (temperature and pressure) on the trapping capacities are discussed in this section.

Figure 11 shows a simple schematic of the energy profile near a hydrogen trap site, similar to that shown in Ref. [77]. In this schematic, hydrogen occupies a trap site, with a binding energy E_b, which is defined as the energy difference between hydrogen in a trap site and in an interstitial site. The detrapping activation energy E_{de} is the sum of the trap binding energy E_b and the diffusion activation energy E_{diff}, i.e., $E_{de} = E_b + E_{diff}$.

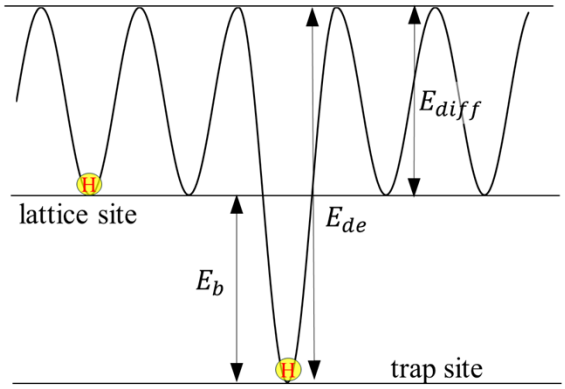

Figure 11. Schematic energy profile near a hydrogen trap site

Based on the Oriani's equilibrium theory [78], the occupancy fraction of a trap site i, denoted as θ_T^i, is related to the lattice site occupancy fraction θ_L and the binding energy E_b^i of the trap site i, as shown in *Eq. 1* [79], where R is the gas constant and T is temperature. This expression describes the thermodynamic equilibrium partitioning of hydrogen between interstitial and trap sites. The trap site occupancy fraction θ_T^i is proportional to the quantity of hydrogen retained by the trap and, therefore, indicative of the trapping capacity under equilibrium conditions .

$$\theta_T^i = \frac{\theta_L exp\left(\frac{E_b^i}{RT}\right)}{1 - \theta_L + \theta_L exp\left(\frac{E_b^i}{RT}\right)} \qquad Eq.\ 1$$

The lattice site occupancy fraction θ_L can be expressed as $\theta_L = C_L/N_L$, where C_L is the hydrogen concentration in the lattice site (unit: mol/m^3), and N_L is the number of interstitial lattice site per unit volume (unit: mol/m^3) [79]. In a body-centered cubic (bcc) structure such as α-Fe, hydrogen preferentially occupies tetrahedral interstitial sites [80]. Each bcc unit cell contains 12 tetrahedral sites and 2 metal atoms, corresponding to 6 tetrahedral sites per matrix atom. Thus, θ_L can be written as: $\theta_L = 1/6 \times C_L/C_m$, where C_m is the molar concentration of matrix atoms (unit: mol/m^3). Using the hydrogen solubility in pure α-Fe from Ref. [81], θ_L can be expressed as *Eq. 2,* assuming the same deuterium solubility as hydrogen, where P is the deuterium pressure, in the unit of atmosphere. Lattice fraction θ_L increases as temperature and pressure increases.

$$\theta_L = 1 \times 10^{-8} exp\left[1.3\ ln(T) - \frac{1750}{T}\right] \times \sqrt{P} \qquad Eq.\ 2$$

As shown by combining *Eq. 1* and *Eq. 2*, the deuterium trapping quantity is a function of charging temperature T, pressure P and binding energy E_b^i. Figure 12a presents the relationship between trap site occupancy fraction θ_T and D_2 gas charging pressure at 450 ˚C for traps with the binding energy ranging from 20 to 120 kJ/mol, covering all trapping sites typically observed in ferritic steels [7, 82]. Deep traps with high binding energy tend to approach saturation, whereas shallow traps with low binding energy are far from saturation. As pressure increases, the trap fraction θ_T also increases, and the fraction becomes less sensitive to pressure change beyond 1 atm. The charging pressure in this study was 1 atm, and all trap site θ_T increase or decrease as pressure changes, maintaining the relative deuterium capacities of different trap sites. Figure 12b shows the effect of D_2 gas charging temperature on trap fraction θ_T at a constant pressure of 1 atm. The occupancy fraction increases as the charging temperature decreases, meaning that deuterium

capacities for all trap sites increase at lower temperatures while maintaining the relative trends discussed in the previous section.

The findings of this study establish a foundational understanding of deuterium trapping behavior in RAFM steels under fusion-relevant conditions. While temperature and pressure variations refine the quantitative trapping response, the observed temperature- and pressure-dependent trapping behaviors offer a critical reference for future studies.

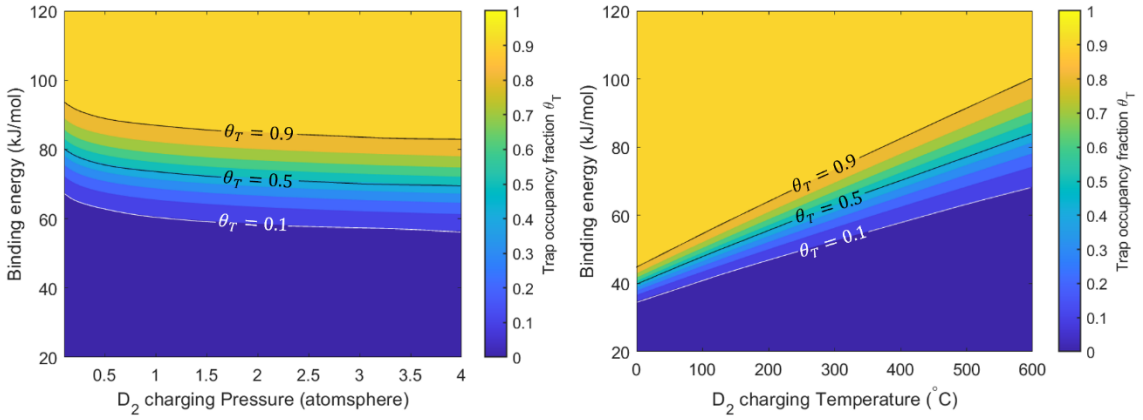

Figure 12. Trap site occupancy fraction θ_T as a function of (a) D_2 charging temperature at 1 atm D_2 pressure and (b) D_2 charging pressure at 450 ˚C.

5. Conclusion

RAFM steels contain multiple intrinsic microstructural features that act as hydrogen trapping sites. Developing stronger materials requires a fundamental understanding of hydrogen trapping mechanisms and trapping capacity of individual microstructure features. This study involved designing and fabricating various model alloys and engineering steels, which were subjected to different heat treatments to control the density of hydrogen trapping sites. Deuterium retention and desorption properties were evaluated using TDS after the D_2 gas charging at 450 °C. Deuterium trapping properties were correlated with sample microstructure, which was comprehensively characterized by EBSD, STEM/EDS, and synchrotron XRD. This work identified the role of dominant microstructure features in deuterium trapping sites and their relationship to mechanical properties.

In RAFM steels, deuterium desorption occurs at different temperatures, representing different trapping mechanisms. Grain boundary and dislocation have lower deuterium desorption temperature (less than about 300 °C), whereas TiC and $M_{23}C_6$ precipitates are responsible for deuterium desorption at high temperature (greater than about 400 °C).

The amount of deuterium trapping depends on the density of trapping sites and their trapping capacity per unit area. Using the linear least-squares fitting on deuterium retention at the D_2 charging condition of 450 ˚C and 760Torr and the areal density of individual trapping sites, TiC precipitates demonstrate highest trapping capacity (6.8×10^{-7} mol/m^2), followed by $M_{23}C_6$ precipitates (7.7×10^{-8} mol/m^2), dislocation (2.2×10^{-8} mol/m^2), and grain boundary (2.0×10^{-8} mol/m^2). In engineering steels (both 9Cr-1TiW-0.05C and 9Cr-1TiW-0.1C), TiC precipitates account for more than about 60% of deuterium trapping, and dislocation and grain boundary contribute similar deuterium trapping, approximately 10%–15% for each feature. The dependency of trapping capacity on charging temperature and pressure are discussed, and the relative trends in deuterium capacity are expected to be maintained across different charging conditions.

Stronger materials generally trap more deuterium: ODS steels demonstrate higher deuterium retention than FM steels and model alloys. Significant variations in deuterium trapping were observed even among materials with similar strength, highlighting the distinct role that different microstructural features play in mechanical strengthening and deuterium trapping. Using the dispersed barrier hardening model to estimate the strengthening contribution from individual microstructure features, TiC precipitates demonstrate the strongest deuterium trapping per unit of strengthening contribution, followed by the $M_{23}C_6$ precipitates, boundary, and dislocation.

Advanced materials development often involves increasing the density of barriers against dislocation movement. This strategy could simultaneously increase hydrogen trapping. This work provides critical insights into the deuterium trapping in various microstructure features in RAFM steels, elucidating the relationship between microstructure and deuterium trapping properties. The results of this work are essential for developing materials that balance both mechanical performance and tritium management in future fusion reactors.

6. Acknowledgment

This work was supported by the US Department of Energy, Office of Fusion Energy Science under contract no. DEAC05-00OR22725 with UT-Battelle, LLC. Use of the National Synchrotron Light Source-II, Brookhaven National Laboratory, was supported by the U.S. Department of Energy under Contract no. DE-SC0012704.

Author Contribution:

W.Z.: Conceptualization; Data curation; Formal analysis; Investigation; Funding acquisition; Writing - original draft;

D.S.: Data curation; Formal analysis. Writing - review & editing.

M.O.: Formal analysis; Writing - review & editing.

L.S: Funding acquisition; Writing - review & editing.

Y.K: Funding acquisition; Supervision; Writing - review & editing

References

[1] M. Aminudin, S. Kamarudin, B. Lim, E. Majilan, M. Masdar and N. Shaari, "An overview: Current progress on hydrogen fuel cell vehicles," *International Journal of Hydrogen Energy,* vol. 48, pp. 4371-4388, 2023.

[2] P. Muthukumar, A. Kumar, M. Afzal, S. Bhogilla, P. Sharma, A. Parida, S. Jana, E. A. Kumar, R. K. Pai and I. Jain, "Review on large-scale hydrogen storage systems for better sustainability," *International Journal of Hydrogen Energy,* vol. 48, pp. 33223-33259, 2023.

[3] R. J. Pearson, A. B. Antoniazzi and W. J. Nuttall, "Tritium supply and use: a key issue for the development of nuclear fusion energy," *Fusion Engineering and Design,* vol. 136, pp. 1140-1148, 2018.

[4] X. Li, X. Ma, J. Zhang, E. Akiyama, Y. Wang and X. Song, "Review of hydrogen embrittlement in metals: hydrogen diffusion, hydrogen characterization, hydrogen embrittlement mechanism and prevention," *Acta Metallurgica Sinica,* vol. 33, pp. 759-773, 2020.

[5] P. Gong, A. Turk, J. Nutter, F. Yu, B. Wynne, P. Rivera-Diaz-del-Castillo and W. M. Rainforth, "Hydrogen embrittlement mechanisms in advanced high strength steel," *Acta Materialia,* vol. 223, p. 117488, 2022.

[6] O. Barrera, D. Bombac, Y. Chen, T. Daff, E. Galindo-Nava, P. Gong, D. Haley, R. Horton, I. Katzarov, J. R. Kermode, C. Liverani, M. Stopher and F. Sweeney, "Understanding and mitigating hydrogen embrittlement of steels: a review of experimental, modelling and design progress from atomistic to continuum," *Journal of materials science,* vol. 53, pp. 6251-6290, 2018.

[7] Y.-S. Chen, C. Huang, P.-Y. Liu, H.-W. Yen, R. Niu, P. Burr, K. L. Moore, E. Martinez-Paneda, A. Atrens and J. M. Cairney, "Hydrogen trapping and embrittlement in metals-A review," *International Journal of Hydrogen Energy,* 2024.

[8] S. J. Zinkle and J. T. Busby, "Structural materials for fission & fusion energy," *Materials today,* vol. 12, pp. 12-19, 2009.

[9] J. Linke, J. Du, T. Loewenhoff, G. Pintsuk, B. Spilker, I. Steudel and M. Wirtz, "Challenges for plasma-facing components in nuclear fusion," *Matter and Radiation at Extremes,* vol. 4, p. 056201 , 2019.

[10] S. J. Zinkle and L. L. Snead, "Designing radiation resistance in materials for fusion energy," *Annual Review of Materials Research,* vol. 44, pp. 241-267, 2014.

[11] W. Zhong and L. Tan, "Radiological analysis and transmutation calculation of representative castable nanostructured alloys," *Fusion Engineering and Design,* vol. 160, p. 111899, 2020.

[12] S. Zinkle, J. Boutard, D. Hoelzer, A. Kimura, R. Lindau, G. Odette, M. Rieth, L. Tan and H. Tanigawa, "Development of next generation tempered and ODS reduced activation ferritic/martensitic steels for fusion energy applications," *Nuclear Fusion,* vol. 57, p. 092005, 2017.

[13] L. Tan, T. Graening, X. Hu, W. Zhong, Y. Yang, S. Zinkle and Y. Katoh, "Effects of carbonitrides and carbides on microstructure and properties of castable nanostructured alloys," *Journal of Nuclear Materials,* vol. 540, p. 152376, 2020.

[14] M. Alinger, G. Odette and D. Hoelzer, "On the role of alloy composition and processing parameters in nanocluster formation and dispersion strengthening in nanostuctured ferritic alloys," *Acta Materialia,* vol. 57, pp. 392-406, 2009.

[15] Z. Liu, G. Xu, Y. Zhang, L. Zhang and J. Huang, "Influence of multiple short-time normalizations on mechanical properties and microstructure of 9Cr-2.3 W-3.0 Co heat-resistant steels," *Materials Science and Engineering: A,* vol. 879, p. 145282, 2023.

[16] L. Pilloni, C. Cristalli, O. Tassa, I. Salvatori and S. Storai, "Grain size reduction strategies on Eurofer," *Nuclear Materials and Energy,* vol. 17, pp. 129-136, 2018.

[17] P. Prakash, J. Vanaja, N. Srinivasan, P. Parameswaran, G. N. Rao and K. Laha, "Effect of thermo-mechanical treatment on tensile properties of reduced activation ferritic-martensitic steel," *Materials Science and Engineering: A,* vol. 724, pp. 171-180, 2018.

[18] L. Tan, J. T. Busby, P. J. Maziasz and Y. Yamamoto, "Effect of thermomechanical treatment on 9Cr ferritic-martensitic steels," *Journal of Nuclear Materials,* vol. 441, pp. 713-717, 2013.

[19] Z. Chen, X. Hu, M. Ye and B. D. Wirth, "Deuterium transport and retention properties of representative fusion blanket structural materials," *Journal of Nuclear Materials,* vol. 549, p. 152904, 2021.

[20] X. Hu, L. Tan, K. Wang, C. P. Massey, D. T. Hoelzer and Y. Katoh, "Deuterium retention in advanced steels for fusion reactor structural application," *Journal of Nuclear Materials,* vol. 516, pp. 144-151, 2019.

[21] D. Di Stefano, R. Nazarov, T. Hickel, J. Neugebauer, M. Mrovec and C. Elsasser, "First-principles investigation of hydrogen interaction with TiC precipitates in alpha-Fe," *Physical Review B,* vol. 93, p. 184108, 2016.

[22] Y.-S. Chen, H. Lu, J. Liang, A. Rosenthal, H. Liu, G. Sneddon, I. McCarroll, Z. Zhao, W. Li, A. Guo and J. Cairney, "Observation of hydrogen trapping at dislocations, grain boundaries, and precipitates," *Science,* vol. 367, pp. 171-175, 2020.

[23] J. Takahashi, K. Kawakami and Y. Kobayashi, "Origin of hydrogen trapping site in vanadium carbide precipitation strengthening steel," *Acta Materialia,* vol. 153, pp. 193-204, 2018.

[24] J. Takahashi, K. Kawakami, Y. Kobayashi and T. Tarui, "The first direct observation of hydrogen trapping sites in TiC precipitation-hardening steel through atom probe tomography," *Scripta Materialia,* vol. 63, pp. 261-264, 2010.

[25] Y.-S. Chen, D. Haley, S. S. Gerstl, A. J. London, F. Sweeney, R. A. Wepf, W. M. Rainforth, P. A. Bagot and M. P. Moody, "Direct observation of individual hydrogen atoms at trapping sites in a ferritic steel," *Science,* vol. 355, pp. 1196-1199, 2017.

[26] J. Fang, C. Xu, Y. Li, R. Peng and X. Fu, "Effect of grain orientation and interface coherency on the hydrogen trapping ability of TiC precipitates in a ferritic steel," *Materials Letters,* vol. 308, p. 131281, 2022.

[27] R. Shi, Y. Ma, Z. Wang, L. Gao, X.-S. Yang, L. Qiao and X. Pang, "Atomic-scale investigation of deep hydrogen trapping in NbC/α-Fe semi-coherent interfaces," *Acta materialia,* vol. 200, pp. 686-698, 2020.

[28] F.-G. Wei, T. Hara and K. Tsuzaki, "Nano-preciptates design with hydrogen trapping character in high strength steel," *Advanced Steels: The Recent Scenario in Steel Science and Technology,* pp. 87-92, 2011.

[29] H. Lee and J.-Y. Lee, "Hydrogen trapping by TiC particles in iron," *Acta Metallurgica,* vol. 32, pp. 131-136, 1984.

[30] S. M. Lee and J. Y. Lee, "The effect of the interface character of TiC particles on hydrogen trapping in steel," *Acta Metallurgica,* vol. 35, pp. 2695-2700, 1987.

[31] P. Yu, Y. Cui, G.-z. Zhu, Y. Shen and M. Wen, "The key role played by dislocation core radius and energy in hydrogen interaction with dislocations," *Acta Materialia,* vol. 185, pp. 518-527, 2020.

[32] I. E. McCarroll, Y.-C. Lin, A. Rosenthal, H.-W. Yen and J. M. Cairney, "Hydrogen trapping at dislocations, carbides, copper precipitates and grain boundaries in a dual precipitating low-carbon martensitic steel," *Scripta Materialia,* vol. 221, p. 114934, 2022.

[33] R. Matsumoto, M. Riku, S. Taketomi and N. Miyazaki, "Hydrogen-grain boundary interaction in Fe, Fe-C, and Fe-N systems," *Prog. Nucl. Sci. Technol,* vol. 2, pp. 9-15, 2011.

[34] L. Cho, P. Bradley, D. Lauria, M. Connolly, E. Seo, K. Findley, J. Speer, L. Golem and A. Slifka, "Effects of hydrogen pressure and prior austenite grain size on the hydrogen embrittlement characteristics of a press-hardened martensitic steel," *international journal of hydrogen energy,* vol. 46, pp. 24424-24439, 2021.

[35] M. Moshtaghi, B. Loder, M. Safyari, T. Willidal, T. Hojo and G. Mori, "Hydrogen trapping and desorption affected by ferrite grain boundary types in shielded metal and flux-cored arc weldments with Ni addition," *International Journal of Hydrogen Energy,* vol. 47, pp. 20676-20683, 2022.

[36] D. Sprouster, J. Sinsheimer, E. Dooryhee, S. Ghose, P. Wells, T. Stan, N. Almirall, G. Odette and L. Ecker, "Structural characterization of nanoscale intermetallic precipitates in highly neutron irradiated reactor pressure vessel steels," *Scripta Materialia,* vol. 113, pp. 18-22, 2016.

[37] P. Scardi, C. L. Azanza Ricardo, C. Perez-Demydenko and A. A. Coelho, "Whole powder pattern modelling macros for TOPAS," *Journal of Applied Crystallography,* vol. 51, pp. 1752-1765, 2018.

[38] D. J. Sprouster, R. Weidner, S. Ghose, E. Dooryhee, T. Novakowski, T. Stan, P. Wells, N. Almirall, G. Odette and L. Ecker, "Infrastructure development for radioactive materials at the NSLS-II," *Nuclear Instruments and Methods in Physics Research Section A: Accelerators, Spectrometers, Detectors and Associated Equipment,* vol. 880, pp. 40-45, 2018.

[39] D. J. Sprouster, W. S. Cunningham, G. P. Halada, H. Yan, A. Pattammattel, X. Huang, D. Olds, M. Tilton, Y. S. Chu, E. Dooryhee, G. P. Manogharan and J. R. o. Trelewicz, "Dislocation

microstructure and its influence on corrosion behavior in laser additively manufactured 316L stainless steel," *Additive Manufacturing,* vol. 47, p. 102263, 2021.

[40] T. Ungar, "Dislocation densities, arrangements and character from X-ray diffraction experiments," *Materials Science and Engineering: A,* vol. 309, pp. 14-22, 2001.

[41] B. Warren and B. Averbach, "The effect of cold-work distortion on X-ray patterns," *Journal of applied physics,* vol. 21, pp. 595-599, 1950.

[42] H. Kitahara, R. Ueji, N. Tsuji and Y. Minamino, "Crystallographic features of lath martensite in low-carbon steel," *Acta materialia,* vol. 54, pp. 1279-1288, 2006.

[43] M. Tamura, H. Kusuyama, K. Shinozuka and H. Esaka, "Tempering process and precipitation behavior of 8% Cr-2% WTa steel," *ISIJ international,* vol. 47, pp. 317-326, 2007.

[44] M. Wilkens, "The determination of density and distribution of dislocations in deformed single crystals from broadened X-ray diffraction profiles," *Physica status solidi (a),* vol. 2, pp. 359-370, 1970.

[45] T. Ungar and A. Borbely, "The effect of dislocation contrast on x-ray line broadening: A new approach to line profile analysis," *Applied Physics Letters,* vol. 69, pp. 3173-3175, 1996.

[46] T. Ungar, A. D. Stoica, G. Tichy and X.-L. Wang, "Orientation-dependent evolution of the dislocation density in grain populations with different crystallographic orientations relative to the tensile axis in a polycrystalline aggregate of stainless steel," *Acta materialia,* vol. 66, pp. 251-261, 2014.

[47] J. J. Adams, D. Agosta, R. Leisure and H. Ledbetter, "Elastic constants of monocrystal iron from 3to500K," *Journal of applied physics,* vol. 100, 2006.

[48] T. Ungar, I. Dragomir, A. Revesz and A. Borbely, "The contrast factors of dislocations in cubic crystals: the dislocation model of strain anisotropy in practice," *Journal of applied crystallography,* vol. 32, pp. 992-1002, 1999.

[49] Y. Dai, T. Man, Z. Wang, Y. Liu, Y. Bao and X. Wei, "The Inclusion Characteristics and Mechanical Properties of M2 High-Speed Steel Treated with a Vacuum Carbon Deoxidation Process," *Metals,* vol. 14, p. 1146, 2024.

[50] R. Kirchheim, "Hydrogen solubility and diffusivity in defective and amorphous metals," *Progress in Materials Science,* vol. 32, pp. 261-325, 1988.

[51] K. Bergers, E. Camisao de Souza, I. Thomas, N. Mabho and J. Flock, "Determination of hydrogen in steel by thermal desorption mass spectrometry," *steel research international,* vol. 81, pp. 499-507, 2010.

[52] F. G. Wei and K. Tsuzaki, "Quantitative analysis on hydrogen trapping of TiC particles in steel," *Metallurgical and Materials Transactions A,* vol. 37, pp. 331-353, 2006.

[53] D. Hull and D. J. Bacon, "Dislocation Arrays and Crystal Boundaries," in *Introduction to dislocations*, Elsevier, 2011, pp. 171-204.

[54] C. Zhao, Y. Xing, C. Zhou and P. Bai, "Experimental examination of displacement and strain fields in an edge dislocation core," *Acta materialia,* vol. 56, pp. 2570-2575, 2008.

[55] G. S. Was, Fundamentals of radiation materials science: metals and alloys, Springer, 2007.

[56] A. Turk, G. R. Joshi, M. Gintalas, M. Callisti, P. E. Rivera-D{\'\i}az-del-Castillo and E. I. Galindo-Nava, "Quantification of hydrogen trapping in multiphase steels: Part I-Point traps in martensite," *Acta Materialia,* vol. 194, pp. 118-133, 2020.

[57] F. W. Wiffen, S. P. Noe and L. L. Snead, "Fusion Materials Research at Oak Ridge National Laboratory in Fiscal Year 2014," Oak Ridge National Laboratory, Oak Ridge, TN (United States), 2014.

[58] Oak Ridge National Laboratory, "FUSION MATERIALS SEMIANNUAL PROGRESS REPORT," Oak Ridge National Laboratory, Oak Ridge, TN, US, ORNL/TM-2023/3142 , 2023.

[59] D. T. Hoelzer, "Summary of Previous Mechanical Test Data on ODS Alloys 14YWT and OFRAC up to 1000C," Oak Ridge National Laboratory, Oak Ridge, TN, US. ORNL/LTR-2021/1910, 2021.

[60] R. Schaeublin, T. Leguey, P. Spatig, N. Baluc and M. Victoria, "Microstructure and mechanical properties of two ODS ferritic/martensitic steels," *Journal of nuclear materials,* vol. 307, pp. 778-782, 2002.

[61] "NIMSCreep Data Sheet No. 43A," National Institute for Materials Science, Japan, 2014. [Online]. Available: https://smds.nims.go.jp/creep/en/.

[62] E. Pavlina and C. Van Tyne, "Correlation of yield strength and tensile strength with hardness for steels," *Journal of materials engineering and performance,* vol. 17, pp. 888-893, 2008.

[63] A. Seeger, J. Diehl, S. Mader and H. Rebstock, "Work-hardening and work-softening of face-centred cubic metal crystals," *Philosophical Magazine,* vol. 2, pp. 323-350, 1957.

[64] L. Tan, W. Zhong and T. Chen, "Microstructural stability of tantalum-alloyed ferritic-martensitic steel with neutron irradiation to 7.4 dpa at ~ 490 C," *Materialia,* vol. 9, p. 100608, 2020.

[65] L. Tan and J. T. Busby, "Formulating the strength factor alpha for improved predictability of radiation hardening," *Journal of Nuclear Materials,* vol. 465, pp. 724-730, 2015.

[66] S. J. Zinkle and Y. Matsukawa, "Observation and analysis of defect cluster production and interactions with dislocations," *Journal of nuclear materials,* vol. 329, pp. 88-96, 2004.

[67] L. Tan, L. L. Snead and Y. Katoh, "Development of new generation reduced activation ferritic-martensitic steels for advanced fusion reactors," *Journal of Nuclear Materials,* vol. 478, pp. 42-49, 2016.

[68] G. Gupta and G. S. Was, "Improved creep behavior of ferritic-martensitic alloy T91 by subgrain boundary density enhancement," *Metallurgical and Materials Transactions A,* vol. 39, pp. 150-164, 2008.

[69] T. Hao, Z. Fan, S. Zhao, G. Luo, C. Liu and Q. Fang, "Strengthening mechanism and thermal stability of severely deformed ferritic/martensitic steel," *Materials Science and Engineering: A,* vol. 596, pp. 244-249, 2014.

[70] X. Zhang, A. Godfrey, X. Huang, N. Hansen and Q. Liu, "Microstructure and strengthening mechanisms in cold-drawn pearlitic steel wire," *Acta Materialia,* vol. 59, pp. 3422-3430, 2011.

[71] X. Zhang, N. Hansen, A. Godfrey and X. Huang, "Dislocation-based plasticity and strengthening mechanisms in sub-20 nm lamellar structures in pearlitic steel wire," *Acta Materialia,* vol. 114, pp. 176-183, 2016.

[72] R. Islamgaliev, M. Nikitina, A. Ganeev and V. Sitdikov, "Strengthening mechanisms in ultrafine-grained ferritic/martensitic steel produced by equal channel angular pressing," *Materials Science and Engineering: A,* vol. 744, pp. 163-170, 2019.

[73] P. Zhu, Y.-R. Lin, S. Agarwal, V. Pauly, S. Taller and S. J. Zinkle, "Comparison of hardening and microstructures of ferritic/martensitic steels irradiated with fast neutrons and dual ions," *Journal of Nuclear Materials,* p. 155211, 2024.

[74] P. Zhu, Y. Zhao, Y.-R. Lin, J. Henry and S. J. Zinkle, "Defect-specific strength factors and superposition model for predicting strengthening of ion irradiated Fe18Cr alloy," *Journal of Nuclear Materials,* vol. 588, p. 154823, 2024.

[75] K. G. Field, X. Hu, K. C. Littrell, Y. Yamamoto and L. L. Snead, "Radiation tolerance of neutron-irradiated model Fe-Cr-Al alloys," *Journal of Nuclear Materials,* vol. 465, pp. 746-755, 2015.

[76] M. Praud, F. Mompiou, J. Malaplate, D. Caillard, J. Garnier, A. Steckmeyer and B. Fournier, "Study of the deformation mechanisms in a Fe-14% Cr ODS alloy," *Journal of Nuclear Materials,* vol. 428, pp. 90-97, 2012.

[77] Y. Hatano, M. Shimada, Y. Oya, G. Cao, M. Kobayashi, M. Hara, B. J. Merrill, K. Okuno, M. A. Sokolov and Y. Katoh, "Retention of hydrogen isotopes in neutron irradiated tungsten," *Materials Transactions,* vol. 54, pp. 437-441, 2013.

[78] R. Oriani and P. Josephic, "Equilibrium aspects of hydrogen-induced cracking of steels," *Acta metallurgica,* vol. 22, no. 9, pp. 1065-1074, 1974.

[79] R. Fernandez-Sousa, C. Betegon and E. Martinez-Paneda, "Analysis of the influence of microstructural traps on hydrogen assisted fatigue," *Acta Materialia,* vol. 199, pp. 253-263, 2020.

[80] H. Wipf, Hydrogen in metals III: properties and applications, Springer, 1997.

[81] N. Shohoji, "Comparative study of solubilities of hydrogen, nitrogen and carbon in alpha-iron," *Journal of materials science,* vol. 21, pp. 2147-2152, 1986.

[82] H. K. D. H. Bhadeshia, "Prevention of hydrogen embrittlement in steels," *ISIJ international,* vol. 56, pp. 24-36, 2016.

[83] Y.-S. Chen, C. Huang, P.-Y. Liu, H.-W. Yen, R. Niu, P. Burr, K. L. Moore, E. Martinez-Paneda, A. Atrens and J. M. Cairney, "Hydrogen trapping and embrittlement in metals--A review," *International Journal of Hydrogen Energy,* 2024.